Switched-Capacitor-Based Hybrid Resonant Bidirectional Buck–Boost Converter for Improving Energy Harvesting in Photovoltaic Systems

Caio Meira Amaral da Luz [1], Kenji Fabiano Ávila Okada [2], Aniel Silva Morais [2], Fernando Lessa Tofoli [1,*] and Enio Roberto Ribeiro [3]

[1] Department of Electrical Engineering, Federal University of São João del-Rei, São João del-Rei 36307-352, Brazil; caiomeiramaral@hotmail.com
[2] Faculty of Electrical Engineering, Federal University of Uberlândia, Uberlândia 38408-100, Brazil; kenji_okada@ufu.br (K.F.Á.O.); aniel@ufu.br (A.S.M.)
[3] Institute of System Engineering and Information Technology, Federal University of Itajubá, Itajubá 37500-903, Brazil; enio.k@unifei.edu.br
* Correspondence: fernandolessa@ufsj.edu.br

Abstract: Photovoltaic (PV) modules are often connected in series to achieve the desired voltage level in practical applications. A common issue with this setup is module mismatch, which can be either permanent or temporary and is caused by various factors. The differential power processing (DPP) concept has emerged as a prominent solution to address this problem. However, a significant drawback of current DPP topologies is their reduced performance under certain conditions, particularly in cases of permanent mismatch. As a result, applications involving the DPP concept for permanent mismatches remain underexplored. In this context, the goal of this work is to develop and implement a novel DPP topology capable of increasing energy harvesting in PV systems under permanent mismatch. The proposed hybrid architecture combines features from both bidirectional buck–boost (BBB) and resonant switched capacitor (ReSC) converters. The ReSC converter operates under soft-switching conditions, minimizing undesirable losses. Key advantages of the proposed converter include fewer switches, lower voltage stress, and soft-switching operation, making it suitable for PV systems with mismatched modules. Experimental tests showed an energy harvesting improvement under the assessed conditions.

Keywords: energy harvesting, mismatch, differential power processing, photovoltaic systems, switched capacitors

1. Introduction

Photovoltaic (PV) systems consist of several interconnected modules designed to convert sunlight into electrical energy. Each module, typically comprising multiple solar cells, captures solar energy and generates direct current (DC) electricity. These modules are connected to form PV arrays, which are further integrated with power electronic converters to manage power flow and convert DC into alternating current (AC) for grid connection or direct usage.

In many situations, PV modules must be connected in series to achieve the required DC voltage level for a specific application [1]. This type of connection is referred to as a PV string. Since the modules are connected in series, the current flowing through all of them must be identical. Since the output current of PV modules increases with the incident solar irradiance, when all elements in a PV string are exposed to the same irradiance level, the power output behaves almost linearly with irradiance [2]. However, if one or more modules generate different currents, a phenomenon known as a mismatch occurs.

As a result, the output power of the PV string no longer follows a linear relationship with irradiance but instead depends on the operating point of each module. Mismatch generally reduces the output power and, in severe cases, can damage the affected module [3].

Mismatch among PV modules is a common issue in PV systems and can be classified as either temporary or permanent. Temporary mismatches are brief and inconsistent, often caused by factors like partial shading or uneven dirt on the module surface [3]. Permanent mismatches, however, result from factors such as differing module orientations, manufacturing variations, aging-related degradation, or connecting modules with different specifications [4].

All of the aforementioned factors lead to a current reduction in the affected modules. As a result, a mismatch occurs when PV modules in a series generate unequal currents. According to Kirchhoff's current law, the current through each module in the series must be the same. Consequently, two key scenarios can arise, depending on the current drawn by the load connected to the PV system.

In the first situation, the current of the shaded PV module limits the entire string, reducing the total energy harvested. However, this scenario does not pose a risk to the module's integrity [5,6]. In the second situation, the current of the PV string is determined by the modules generating a higher current. This forces the affected module into the reverse bias region, where it operates with a positive current and a negative voltage. Thus, the module behaves like a resistor, consuming energy from its neighboring counterparts. This energy is dissipated as heat, leading to the formation of hot spots [3]. In more severe mismatch conditions, this can cause irreparable damage to the PV modules in the string.

The bypass diode is the most widely adopted strategy to prevent the formation of hot spots [7]. It is connected in anti-parallel to the strings of PV cells in a module, or even to the entire module. When a mismatch occurs and one or more modules enter the reverse bias region, the bypass diode becomes forward-biased [5,8]. This provides a low-resistance path for the current, bypassing the mismatched module. Consequently, the power from the affected module is lost, reducing the overall efficiency of the PV system [9]. Additionally, the mismatched module will operate at a different voltage level, leading to the generation of multiple peaks, with one global maximum power point (GMPP) and several local maximum power points (LMPPs). As a result, conventional maximum power point tracking (MPPT) algorithms, such as perturb and observe (P&O) and incremental conductance (InC), are unable to track the GMPP, leading to further energy harvesting losses [10–12].

In recent years, various mismatch mitigation strategies based on power electronics have been proposed [3,13,14]. These solutions typically include DC optimizers [14,15], microinverters [16], and partial or differential power processing (DPP) converters [17–20]. The main advantage of these distributed power electronics approaches is their ability to mitigate mismatch effects, thereby increasing the overall energy harvested by the PV system. Additionally, they improve system reliability by reducing the risk of hot spots. However, a significant drawback of DC optimizers and microinverter architectures is their reliance on full power processing (FPP), requiring each converter to handle the full output power of its corresponding PV module, which increases losses and size. In contrast, the DPP concept has emerged as a promising solution due to its advantages in energy recovery, simple implementation, and cost-effectiveness [20,21]. This approach was introduced in [22], with its mathematical analysis and practical feasibility assessed in [23]. Notably, partial power processing (PPP) converters are generally inferior to DPP architectures in PV systems because PPP converters process a larger proportion of the total power flow compared to DPP.

The DPP concept has emerged as a promising alternative, offering significant improvements in efficiency, reliability, and cost compared to conventional solutions. It was introduced in [22], with its first experimental validation conducted in [23]. In this approach, bidirectional DC–DC converters, known as DPP converters, are connected in parallel with the PV modules in the string. Unlike FPP, DPP converters operate only when

needed and process only a small fraction of the total system power, typically a small percentage of the overall output [24]. This results in higher system efficiency, smaller size, and reduced power ratings for the power electronics components. Depending on the arrangement of DPP converters in the PV string, three main architectures can be identified: PV-to-PV, PV-to-bus, and hybrid, as shown in Figure 1a–c, respectively [25,26].
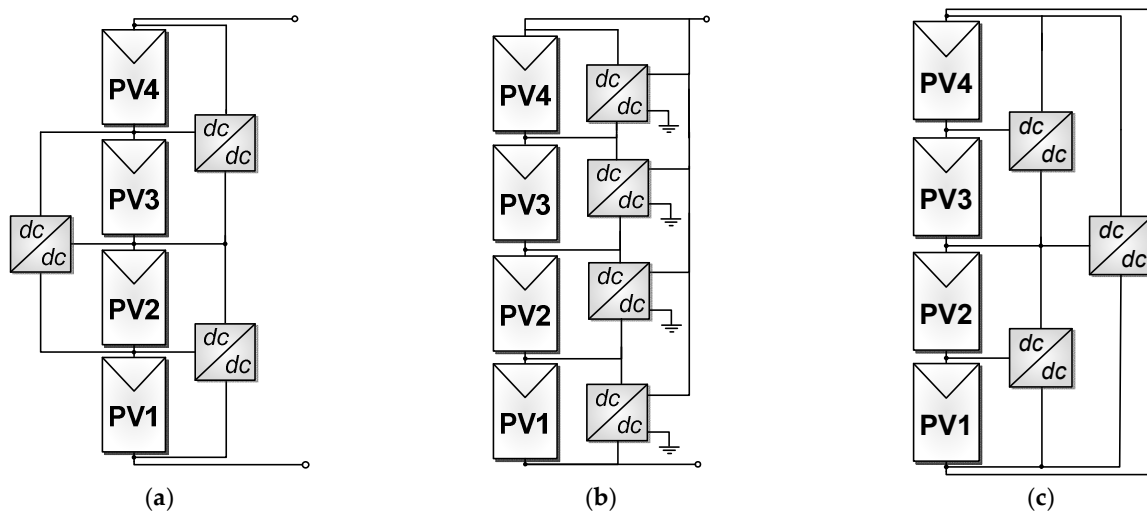

Figure 1. DPP arrangements: (**a**) PV-to-PV architecture, (**b**) PV-to-bus architecture, and (**c**) hybrid architecture.

In the PV-to-PV architecture depicted in Figure 1a, DPP converters are modularly connected to the PV modules, which are in turn connected series [23]. In this setup, the number of DPP converters is always one less than the number of PV modules. A key advantage is that the maximum voltage stress on the switches is only twice the open-circuit voltage of the PV modules [13]. However, due to the modular nature of the PV-to-PV architecture, energy is shared among a given PV module and its neighboring modules. This results in the diverted current accumulation phenomenon [27], where all converters in the PV-to-PV system are activated even if only one module is mismatched. The two most commonly used DC–DC converters in this architecture are the bidirectional buck–boost converter [26–28] and the switched-capacitor converter [29,30].

In the PV-to-bus architecture represented in Figure 1b, DPP converters are connected between each PV module and the main bus, resulting in the number of DPP converters being equal to the number of PV modules. In this architecture, power is exchanged directly between the PV module and the main bus, so only one converter is required to compensate for a mismatch. Consequently, the phenomenon of diverted current accumulation does not occur in this setup [27]. However, a drawback is that the secondary-side switches of the converter must be rated for the full bus voltage, and under certain conditions, more power is processed [24,31]. To reduce the high voltage stress, some studies have proposed an improved architecture called PV-to-Isolated-Bus, where the secondary side of the DC converter is decoupled from the main bus [32]. In this case, when a mismatched module needs compensation, matched modules deliver power through two converters: their own and the mismatched module's converter [32,33]. However, this limits their energy transfer capability and still requires an isolated DC–DC topology, typically a flyback converter, which increases losses, size, and cost [13].

To address the drawbacks of the two aforementioned architectures, some studies have proposed a hybrid architecture, as shown in Figure 1b [34–36]. In this approach, $n - 1$ DPP converters are required for n PV modules. This configuration mitigates both the issue of diverted current accumulation found in the PV-to-PV architecture and the high voltage stress problem associated with the PV-to-bus architecture. Consequently, this

hybrid architecture is suitable for applications involving permanent mismatch types, as demonstrated in this work.

Despite their constructive differences, these configurations share a fundamental operational principle: equalizing the voltages of the modules around a specific operating point [13]. The converters in these architectures, referred to as DPP converters, temporarily store energy from mismatches in their inductors or capacitors and then release it as current at the PV string output, compensating for current mismatches between modules. This strategy is also known as current diverters [37] and voltage equalizers in [13]. A key advantage of this approach is that when there is no mismatch, the entire system's power is processed solely by a central converter, while DPP converters handle only the differential power resulting from mismatches, typically a fraction of the total PV string power. This results in higher efficiency, reduced size, and lower current and voltage stresses on the components used in DPP converters [38].

Although the DPP concept offers many advantages for mismatch mitigation, few studies focus on permanent mismatches, especially those arising from modules with different specifications. This study is significant because various factors may necessitate the replacement of individual modules over the lifetime of a PV system. In cases of permanent mismatch, the traditional bypass diode strategy is ineffective. To address the challenges posed by permanent mismatches, particularly in PV modules with differing specifications, this work proposes an enhanced DPP topology. Notably, DPP converters in PV systems contribute to sustainability by increasing energy efficiency, extending system lifespan, reducing material use, enhancing energy storage integration, and enabling the scalable deployment of solar energy solutions.

The design is based on the topology developed in [35], which offers significant advancements over previously reported structures. It features a hybrid architecture that combines bidirectional buck–boost (BBB) and SC converters. Its key advantages include eliminating the need for coupled inductors and attenuating the diverted current accumulation. Additionally, unlike most DPP topologies, which are implemented at the sub-module level, this design can be applied at the PV module level. However, a notable drawback of the topology reported in [35] is hard-switching operation, which is due to the switched capacitors. To address this issue, the proposed topology incorporates a simple inductor in series with the capacitor, creating a resonant circuit that operates similarly to a resonant switched-capacitor converter (ReSC). This enables zero-current switching (ZCS) operation and mitigates switching losses.

The remainder of this article is organized as follows. The theoretical analysis of the proposed topology is presented in Section 2. Section 3 describes the experimental setup and discusses the results obtained from a four-module string under two mismatch conditions. Additionally, extending the DPP architecture to larger strings is investigated. A thorough analysis of the solution, including its potential advantages and disadvantages, is also provided. Finally, the conclusion is given in Section 4.

2. DPP Converters

Figure 2 shows the proposed topology, which includes an inductor placed in series with a flying capacitor, forming a resonant circuit that allows the switches to operate under ZCS conditions. To clarify the converter's operating principle, let us consider a PV string divided into two groups: PVG1 and PVG2, each containing two PV modules. Each group is connected in parallel with a BBB converter. The connection between the PV groups is established through a resonant circuit that functions similarly to the ReSC converter.
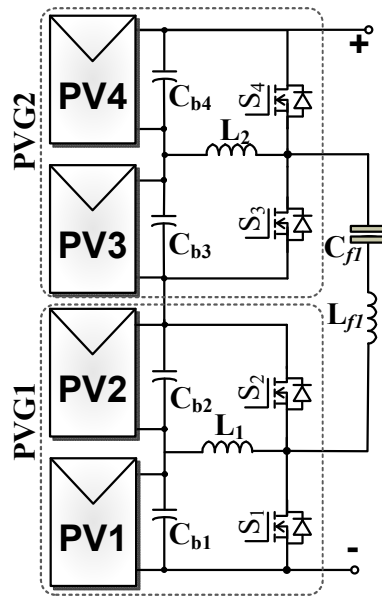
Figure 2. Proposed topology.

2.1. BBB Converter

Figure 3a shows the BBB converter associated with group PVG1 in Figure 2. Assuming a mismatch condition where the current generated by PV module PV2 is less than the current of PV module PV1 at its maximum power point (MPP), corresponding to $I_{PV2} < I_{PV1}$, the following operating modes are observed:
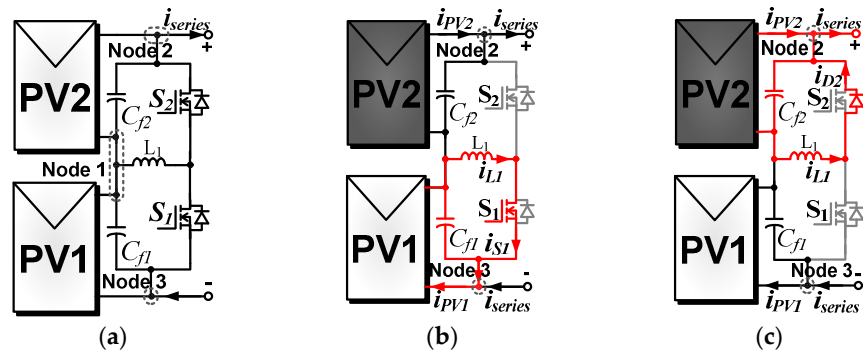

Figure 3. BBB converter operation: (**a**) PV string connected to the BBB converter; (**b**) first stage; and (**c**) second stage.

- First stage [t_0, t_1], Figure 3b: switch S_1 is on and switch S_2 is off. The differential current, given by $\Delta I = I_{PV1} - I_{PV2}$, flows through inductor L_1 and S_1 as observed in Figure 4. As a result, inductor L_1 stores part of the energy harvested by the unshaded module.
- Second stage [t_1, t_2], Figure 3c: switch S_1 is off and switch S_2 is on, while the energy stored in inductor L_1 is released through the diode body of S_2, according to the waveforms depicted in Figure 4.
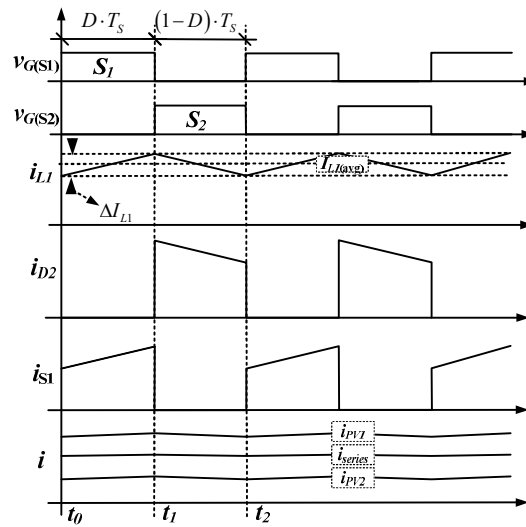
Figure 4. Main waveforms of the BBB converter.

The average current $I_{L1(avg)}$ through the filter inductor of the BBB converter can be determined by the difference in currents between adjacent PV modules, i.e., $I_{L1(avg)} = \Delta I = I_{PV1} - I_{PV2}$. The current ripple, denoted as ΔI_{L1} in (1), is expressed in terms of the duty cycle D, the open-circuit voltage V_{OC}, the filter inductance L_1, and the switching frequency f_S.

$$\Delta I_{L1} = \frac{D V_{OC}}{L_1 f_s} \tag{1}$$

Since the duty ratio is $D = 0.5$, the BBB converter behaves as a voltage equalizer. As a result, each switch only remains on for half of the switching period T_s according to the behavior of the instantaneous currents through D_2 and S_2 represented by i_{D2} and i_{S2}, respectively, in Figure 4. Thus, it is possible to determine the root mean square (RMS) current through the inductor and the switches from (2) and (3), respectively.

$$I_{L1(RMS)} = I_{L1(avg)} \tag{2}$$

$$I_{S1(RMS)} = I_{D2(RMS)} = \frac{I_{L1(avg)}}{\sqrt{2}} \tag{3}$$

Capacitors $C_{b1} \ldots C_{b4}$ act as filter elements in steady state, while the voltages across the modules are constant, and the average currents through the capacitors are zero. Thus, by applying Kirchhoff's current law to node 1 in Figure 3a, the average current through the PV string can be given by (4).

$$I_{string} = \frac{I_{PV1} + I_{PV2}}{2} \tag{4}$$

It can be concluded that the average current through the PV string consists of the combined contribution of the currents from both PV modules. Unlike the bypass diode strategy, which only protects the module, the DPP converter enables the output power of the PV string to benefit from the energy harvested from both modules.

2.2. ReSC Converter

Figure 5 shows the ReSC converter associated with the group of PV modules. For the sake of simplicity, part of BBB converter formerly illustrated in Figure 1 is omitted in Figure 5, as this circuit is not involved in the ReSC converter operation. Notably, the ReSC

converter is not capable of perfectly equalizing the voltage between the PV groups. This is due to the inherent effective impedance that arises as a result of its operation. Therefore, for an initial analysis, a mismatch condition is assumed, where the voltage on PVG2 is given by the sum of the voltages of the two PV modules that compose it, i.e., $V_{PVG2} = V_{PV3}$ + V_{PV4} is lower than the voltage across group PVG2, given by $V_{PVG1} = V_{PV1} + V_{PV2}$. Since V_{PVG2} < V_{PVG1}, the following conditions exist:

- First stage [t_0, t_1], Figure 5b: switches S_1 and S_3 are on, and switches S_2 and S_4 are off. The resonant circuit is connected in parallel with group PVG1 and part of its energy is temporarily stored in the resonant tank, consisting of L_r and C_r.
- Second stage [t_1, t_2], Figure 5b: switches S_1 and S_3 are off, and switches S_2 and S_4 are on. The resonant circuit remains in parallel with the modules of group PVG2. The energy stored in the resonant tank in the previous stage flows through the body diode of S_4 and to balance the current of the mismatched modules, as illustrated in Figure 6.
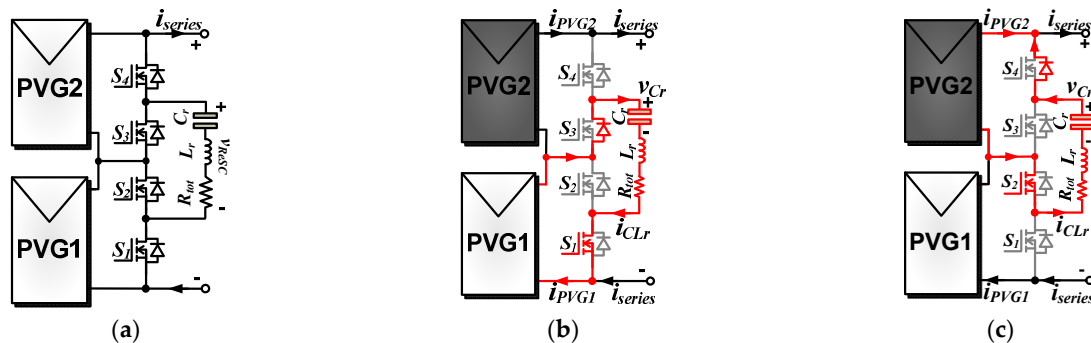

Figure 5. ReSC converter operation: (**a**) PV string connected to the ReSC converter; (**b**) first stage; and (**c**) second stage.
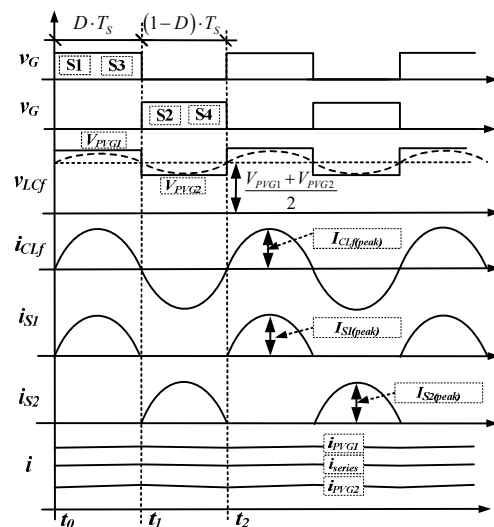

Figure 6. Main waveforms of the ReSC converter.

Since the voltages of the PV modules are unequal, the voltage across the resonant tank has a square waveform, illustrated by v_{LCf} in Figure 6. In this case, the instantaneous voltage across the resonant tank $v_{ReSC}(t)$ must be determined using the Fourier series represented in (5), where h is the harmonic order, while V_{PVG1} and V_{PVG2} stand for the voltages across groups PVG1 and PVG2, respectively.

$$v_{\text{ReSC}}(t) = \frac{V_{PVG1} + V_{PVG2}}{2} + \frac{2(V_{PVG1} - V_{PVG2})}{\pi} \sum_{h=1}^{\infty} \frac{1}{h} \sin\left(\frac{2h\pi}{T_s} t\right) \qquad (5)$$

Considering that the resonant circuit has a high quality factor and operates at the fundamental resonant frequency expressed by (6), it is possible to simplify (5) as (7).

$$f_0 = \frac{1}{2\pi \sqrt{L_f C_f}} \qquad (6)$$

$$v_{\text{ReSC}}(t) = \frac{V_{PVG1} + V_{PVG2}}{2} + \frac{2(V_{PVG1} - V_{PVG2})}{\pi} \sin\left(\frac{2\pi}{T_s} t\right) \qquad (7)$$

The current flowing through the switches and the resonant tank can be obtained using Ohm's law, by dividing (7) by the respective impedances of the resonant circuit for the various frequencies involved. The first harmonic component of $v_{\text{ReSC}}(t)$ has a frequency of zero, so the impedance of the resonant circuit for this component is infinite, resulting in no DC current flow. Conversely, an AC component at a frequency f_0, for which the impedance is $|R_{tot}|$. Thus, the AC current is given by (8).

$$i_{CLf}(t) = \frac{2(V_{PVG1} - V_{PVG2})}{\pi R_{tot}} \sin\left(\frac{2\pi}{T_S} t\right) \qquad (8)$$

The instantaneous current $i_{CLf}(t)$ shown in Figure 6 exhibits a purely sinusoidal behavior. Thus, it is possible to calculate the peak and RMS values of the current through the resonant tank from (8), yielding (9) and (10), respectively.

$$I_{CLf(\text{pk})} = \frac{2(V_{PVG1} - V_{PVG2})}{\pi R_{tot}} \qquad (9)$$

$$I_{CLf(\text{RMS})} = \frac{1}{\sqrt{2}} \frac{2(V_{PVG1} - V_{PVG2})}{\pi R_{tot}} \qquad (10)$$

where R_{tot} represents the sum of resistances from the components constituting the resonant tank, as illustrated in Figure 6a.

According to the waveforms of i_{S1} and i_{S2}, corresponding to the instantaneous currents through the switches in Figure 6, each switch is on for only half of the switching period. Consequently, the peak, RMS, and average currents through the switches are expressed by (11)–(13), respectively.

$$I_{S1(\text{pk})} = I_{S2(\text{pk})} = I_{S3(\text{pk})} = I_{S4(\text{pk})} = \frac{2(V_{PVG1} - V_{PVG2})}{\pi R_{tot}} \qquad (11)$$

$$I_{S1(\text{RMS})} = I_{S2(\text{RMS})} = I_{S3(\text{RMS})} = I_{S4(\text{RMS})} = \frac{(V_{PVG1} - V_{PVG2})}{\pi R_{tot}} \qquad (12)$$

$$I_{S1(\text{avg})} = I_{S2(\text{avg})} = I_{S3(\text{avg})} = I_{S4(\text{avg})} = \frac{2(V_{PVG1} - V_{PVG2})}{\pi^2 R_{tot}} \qquad (13)$$

For PV system applications, it is useful to express the diverted current as a function of the differential current between the PV modules. To do this, determining the effective impedance of the ReSC converter is crucial. According to [39], this parameter is given by $Z_{EFF} = (R_{tot} \pi^2)/4$. Thus, using Ohm's law, one can obtain (14).

$$V_{PVG1} - V_{PVG2} = Z_{EFF(SC)}\left(I_{PVG1} - I_{PVG2}\right) = R_{tot}\frac{\pi^2}{4}\Delta I_{PVG} \tag{14}$$

where ΔI_{PVG} is the differential current between the average current from groups of modules PVG1 and PVG2.

Substituting (14) in (9)–(13) yields (15)–(19).

$$I_{CLf(\text{pk})} = \frac{\pi}{2}\Delta I_{PVG} \tag{15}$$

$$I_{CLf(\text{RMS})} = \frac{\pi}{2\sqrt{2}}\Delta I_{PVG} \tag{16}$$

$$I_{S1(\text{pk})} = I_{S2(\text{pk})} = I_{S3(\text{pk})} = I_{S4(\text{pk})} = \frac{\pi}{2}\Delta I_{PVG} \tag{17}$$

$$I_{S1(\text{RMS})} = I_{S2(\text{RMS})} = I_{S3(\text{RMS})} = I_{S4(\text{RMS})} = \frac{\pi}{4}\Delta I_{PVG} \tag{18}$$

$$I_{S1(\text{avg})} = I_{S2(\text{avg})} = I_{S3(\text{avg})} = I_{S4(\text{avg})} = \frac{1}{2}\Delta I_{PVG} \tag{19}$$

2.3. Proposed Topology

After analyzing each converter individually, the operation of the proposed topology can be investigated. It is important to note that since both converters in the architecture share the same switches, the current stress on these switches will depend on the mismatch conditions. For a clearer understanding, two important mismatch situations need to be analyzed:

➢ In the first case, the two PV modules within one of the PV groups match each other, but mismatch the modules in the other PV group. Since there is no mismatch between the modules within the PV group, the BBB converter will not operate, and only the ReSC will function. Consequently, the behavior of the proposed circuit will be similar to that of the ReSC converter alone. Thus, the current stress on the switches and the resonant tank is described by (15)–(19).

➢ In the second case, the PV modules within one of the groups are mismatched. As a result, both the BBB and ReSC converters will operate. Consequently, the current stress on the switches is the sum of the currents from both converters. This situation is illustrated in Figure 7 for switch S_1, whose peak, RMS, and average currents are given by (20) and (21), respectively.

$$I_{S1(\text{pk})} = I_{S1\_ReSC(\text{pk})} + I_{L1\_BBB(\text{avg})} \tag{20}$$

$$I_{S1(\text{avg})} = I_{S1\_ReSC(\text{avg})} + I_{S1(\text{avg})} \tag{21}$$

$$I_{S1(\text{RMS})} = I_{S1\_ReSC(\text{RMS})} + I_{L1\_BBB(\text{avg})} \tag{22}$$
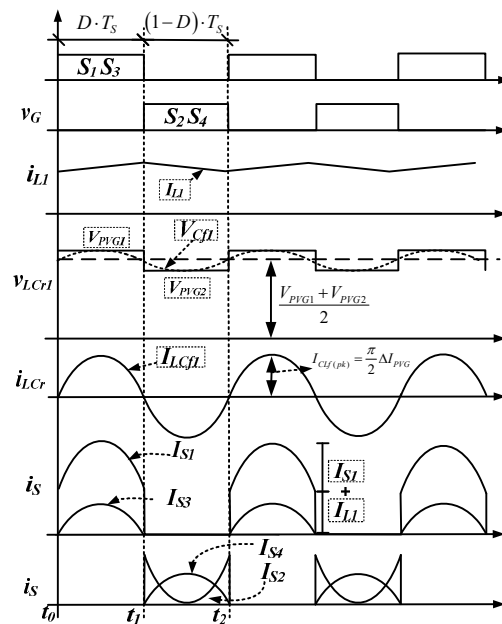
Figure 7. Main waveforms of the proposed topology.

It is important to note that this situation assumes that module PV1 is mismatched. For other mismatch conditions, the peak currents will occur in different switches. Consequently, all switches must be rated for the worst-case scenario, as described by (20) and (21). The voltage stress on the active semiconductors will be the sum of the open-circuit voltages of the adjacent PV modules.

3. Results and Discussion

3.1. Experimental Results Obtained from a Four-Module String

As mentioned, a significant cause of permanent mismatch stems from connecting PV modules with different characteristics. Consider a PV string composed of four 10 W modules, whose total power at standard test conditions (STC) is 40 W. If one element is damaged and must be replaced with a 20 W module due to the unavailability or higher cost of 10 W units, for instance, the dynamics of the string will change.

To demonstrate the operation of the proposed topology and verify the theoretical analysis, an experimental prototype for a PV string with four modules was designed and tested. A mismatch condition involving two PV modules from different manufacturers was considered in terms of one PV module model RSM020P by Resun and one PV module model KS-10 by Kyocera. The main specifications at STC for both elements are presented in Table 1.

Table 1. Electrical characteristics of RSM020P and KS-10 modules.

Parameter	RSM020P	KS-10
Open-circuit voltage	V_{OC} = 21.60 V	V_{OC} = 21.7 V
Short-circuit current	I_{SC} = 1.23 A	I_{SC} = 0.62 A
Voltage at the MPP	V_{MPP} = 18.2 V	V_{MPP} = 17.4 V
Current at the MPP	I_{MPP} = 1.12 A	I_{MPP} = 0.57 A
Maximum power	P_{MPP} = 20 W	P_{MPP} = 10 W

To design the proposed converter, the equations derived in the previous section can be used. According to (1), the main parameters for designing the inductor of the BBB converter include the duty ratio, which for a voltage equalizer is D = 0.5, the open-circuit

voltage V_{OC}, the current ripple ΔI_{L1}, and the switching frequency f_s. In the tests, the following parameters have been adopted: f_s = 50 kHz and V_{OC} = 21.7 V. To calculate the current ripple, the average current is required, which is the difference between the MPP currents of the adjacent mismatched PV modules. In this case, the average current $I_{L1(avg)}$ = 0.55 A is obtained from Table 1. Adopting a maximum current ripple of 10% yields ΔI_{L1} = 10%·$I_{L1(avg)}$. Based on these specifications, the resulting inductance is L_1 = 3.2 mH.

According to Equation (6), the main parameter needed to calculate the resonant tank elements is the switching frequency f_s. Since the BBB and ReSC converters share the same switches in the proposed topology, the switching frequency for both converters is f_s = 50 kHz, as mentioned earlier. With a flying capacitance C_f = 1 µF, a flying inductance L_f = 10 µH is obtained. The voltage stress across the switches is twice the voltage of the adjacent PV modules, with the maximum voltage stress V_{max} = 43.3 V obtained from Table 1. Therefore, the metal-oxide-semiconductor field-effect transistor (MOSFET) model IPP082N10NF2 by Infineon was selected, as its specifications meet the design requirements. All parameters relevant to the implementation of the proposed topology are listed in Table 2, and Figure 8 shows the experimental prototype, which has the same specifications as the setup used in [40].

Table 2. Specifications of the experimental prototype [40].

| Parameter	Specification
Switching frequency	f_s=50 kHz
Maximum current ripple and characteristics of the filter inductors of the BBB converters	ΔI_{L1} = 10%·$I_{PV(max)}$, $L_1 = L_2 = L_3$ = 3.2 mH, ferrite core NNE-30/15/7 by Thornton, 8 × AWG30, 42 turns, $R_L \approx 0.15$ Ω
Filter capacitor C_b	ΔV_{Cb} = 5%·$V_{PV(min)}$, electrolytic capacitor model B41822 by Siemens, 150 µF/100 V, ESR ≈ 300 mΩ
Resonant capacitor C_r	Metalyzed polyester capacitor model MKT368 by Philips, 1 µF/100 V, ESR ≈ 48 mΩ
Resonant inductor L_r	$L_{r1} = L_{r2}$ = 10 µH, ferrite core NT-27/16/12 by Thornton, 10 × AWG30, 10 turns, $R_L \approx 22$ mΩ
Switches	MOSFET IPP082N10NF2 by Infieon, $R_{ds(on)}$ = 8.2 mΩ
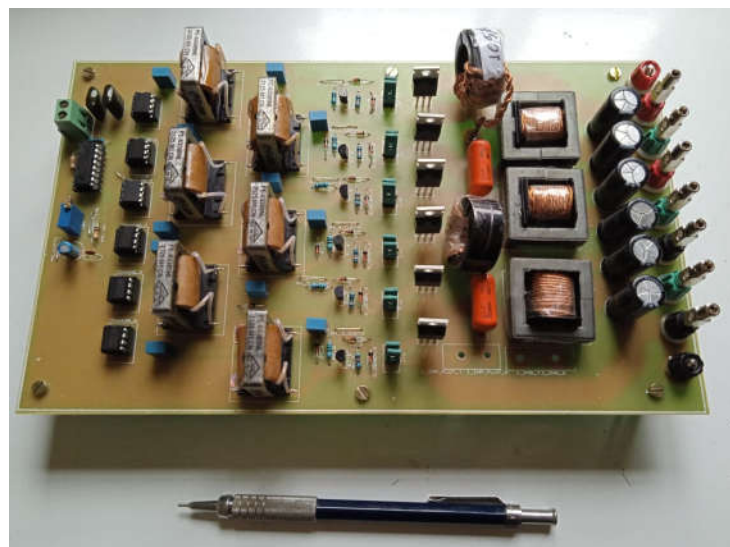
Figure 8. Experimental prototype.

The test bench illustrated in Figure 9 also comprises a PV string composed of four modules, subjected to two mismatch scenarios:

- Scenario 1: connection of two PV modules, model RSM020P, each rated at 20 W, in the PVG1 group, and two PV modules, model KS-10, each rated at 10 W, in the PVG2 group. As a result, the total maximum power of the PV string, which is the sum of the power from all modules, is 60 W.
- Scenario 2: connection of one PV module, model RSM020P, rated at 20 W, at the bottom of the PV string, while the other PV modules in the string are model KS-10, each rated at 10 W. As a result, the maximum power output of the PV string is 50 W.

It is well known that the operating point of the PV string varies with weather conditions, such as irradiance and temperature. To ensure that the PV system operates at its MPP during testing, a variable resistor is used for simplicity.
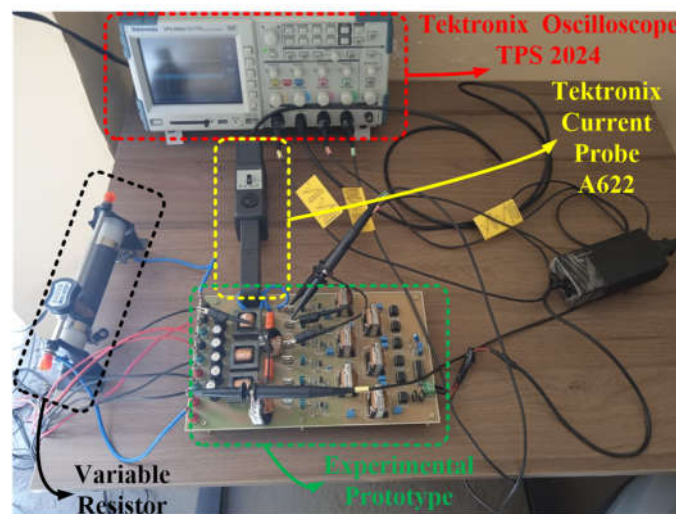

Figure 9. Experimental setup.

3.1.1. Scenario 1

Considering the current at the MPP as mentioned in Table 1, the differential current between the PV module groups is ΔI_{PVG} = 550 mA, which is also reflected in the current versus voltage (*I–V*) curve of the PV modules during testing, as shown in Figure 10. The peak current in the resonant circuit can be determined using (15), resulting in $I_{Clf(pk)}$ = 864 mA. This calculated value is consistent with the experimental result corresponding to the waveform of the resonant tank current in Figure 11a. Other current ratings were also calculated and compared with the experimental results presented in Table 3. Notably, ZCS commutation was observed. Additionally, Figure 11a shows that the voltage stress on the switches is 33.6 V, which aligns with the theoretical analysis, as this value corresponds to the sum of the operating voltages of the modules adjacent to each switch.
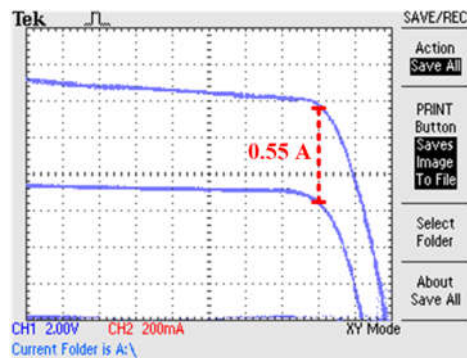
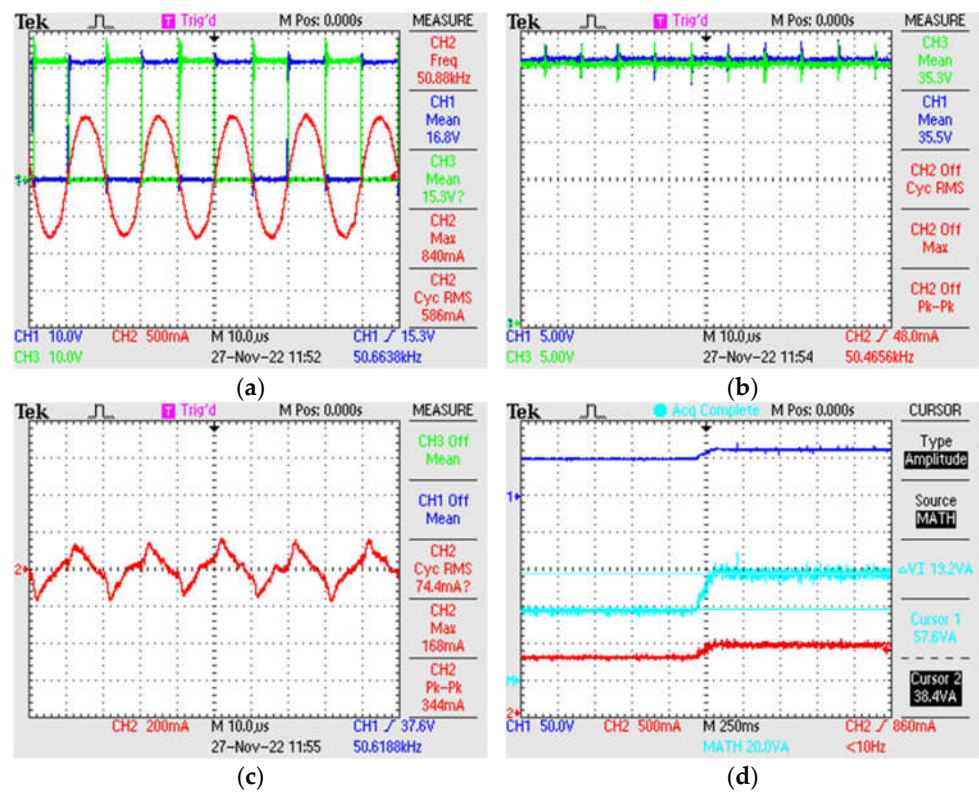**Figure 10.** The *I–V* characteristic of the two PV modules measured during the tests.

Figure 11. Experimental results: (**a**) current in the resonant circuit (red), drain-to-source voltage on switch S_1 (green), drain-to-source voltage on switch S_2 (blue); (**b**) voltage of groups PVG1 (green) and PVG2 (blue). (**c**) current through the inductor of the BBB converter associated with group PVG1 (red); and (**d**) voltage (blue), current (red), and power (cyan) of the PV string before and after operation of the BBB-ReSC topology.

Table 3. Comparison of calculated, simulated, and experimental currents for the first scenario.

Parameter	Quadro		
	Calculated	Simulated	Experimental
$I_{CLf(pk)}$	0.864 A	0.841 A	0.840 A
$I_{CLf(RMS)}$	0.611 A	0.581 A	0.586 A
$I_{S1(pk)}$, $I_{S2(pk)}$, $I_{S3(pk)}$, $I_{S4(pk)}$	0.863 A	0.871 A	0.840 A
$I_{S1(RMS)}$, $I_{S2(RMS)}$, $I_{S3(RMS)}$, $I_{S4(RMS)}$	0.432 A	0.433 A	0.420 A
$I_{S1(avg)}$, $I_{S2(avg)}$, $I_{S3(avg)}$, $I_{S4(avg)}$	0.367 A	0.371 A	0.370 A
$I_{L1(avg)}$, $I_{L2(avg)}$	0 A	0 A	0 A

Figure 11b shows the voltages of the PV groups PVG1 and PVG2. As expected, the voltages across the groups are nearly identical due to the voltage equalization process achieved by the switch operation at a duty ratio of 50%. Since there is no mismatch between the PV modules within each group, the average current in the inductors of the BBB converters is zero. This characteristic is evidenced by the current waveform shown in Figure 11c.

Figure 11d illustrates the voltage, power, and current waveforms before and after the operation of the proposed converter. Initially, the load is adjusted to operate at the MPP of the PV string without the proposed topology connected. In this condition, the maximum output power of the PV string is 38.4 W at an irradiance of 1050 W/m² and a temperature of 45 °C. After activating the topology, the harvested power increases from 38.4 W to 57.6 W, resulting in an increase of 19.2 W, or approximately 50%. Given that efficiency is the ratio of actual output power to the maximum theoretical power that can be harvested from the string, this leads to an increase in efficiency from 64% to 96%.

3.1.2. Scenario 2

Since the PV modules of group PVG1 are mismatched, the respective BBB converter will operate, diverting the differential current caused by the mismatch. This is illustrated in Figure 12c, where the average measured diverted current is 544 mA. The current provided by the mismatched PVG1 group must be determined to calculate the peak current in the resonant tank. The resulting value, obtained from the average current of the two PV modules in the PVG1 group according to (4), is approximately 810 mA, as shown in Table 1. Thus, the differential current between the groups is $\Delta I_{PVG} = 290$ mA. Consequently, using (15), the peak current in the resonant tank is $I_{Clf(pk)} = 455$ mA, which aligns with the experimental results presented in Figure 11a.
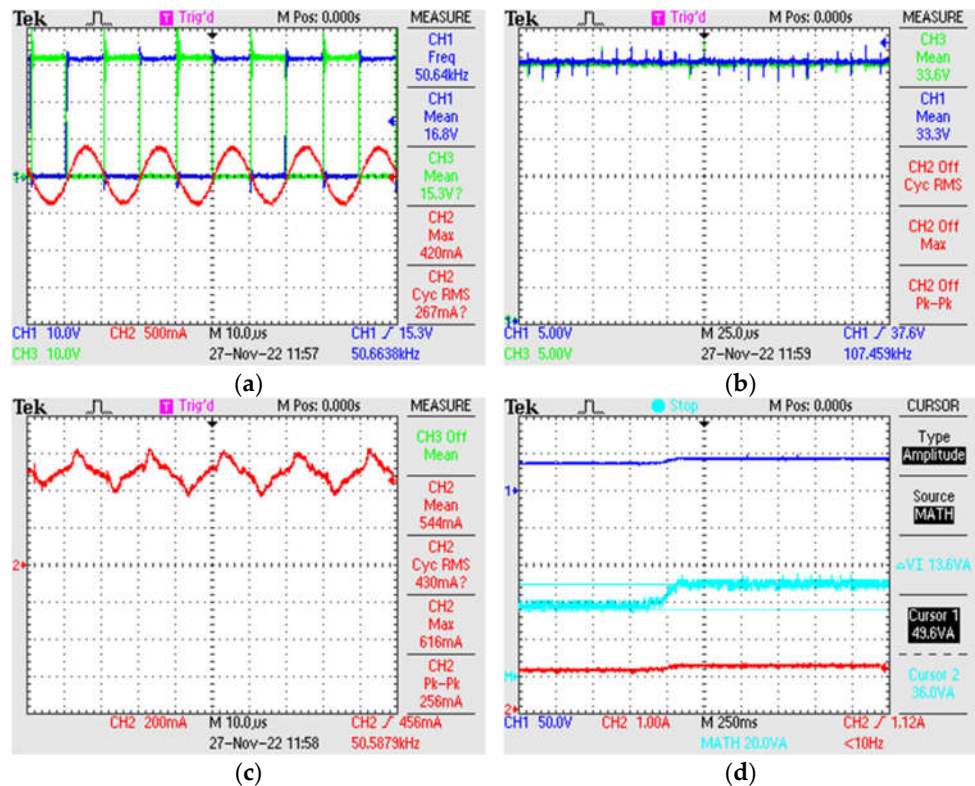

Figure 12. Experimental results: (**a**) current in the resonant circuit (red), drain-to-source voltage on switch S_1 (green), drain-to-source voltage on switch S_2 (blue); (**b**) voltages on groups PVG1 (green) and PVG2 (blue); (**c**) current through the inductor of the BBB converter associated with group PVG1

(red); and (**d**) voltage (blue), current (red), and power (cyan) of the PV string before and after operation of the BBB-ReSC topology.

According to (20), the sum of the average currents diverted by the BBB and ReSC converters is equal to the peak current in the switches of group PVG1. The peak current of the PVG2 group remains equal to that of the resonant tank, as given by (17). Table 4 compares the calculated, simulated, and experimentally measured current values. Additionally, Figure 12a shows that the voltage stress on all the switches in the topology is approximately 33.6 V, which is consistent with the values predicted by the mathematical analysis.

Table 4. Comparison of calculated, simulated, and experimental currents for the second scenario.

Parameter	Quadro		
	Calculated	Simulated	Experimental
$I_{CLf(pk)}$	0.455 A	0.446 A	0.420 A
$I_{CLf(RMS)}$	0.314 A	0.305 A	0.297 A
$I_{L1(avg)}$	0.550 A	0.550 A	0.544 A
$I_{S1(pk)}$	0.982 A	0.996 A	0.964 A
$I_{S1(RMS)}$	0.690 A	0.600 A	0.590 A
$I_{S1(avg)}$	0.09 A	0.1 A	0.110 A
$I_{S2(RMS)}$	0.170 A	0.218 A	0.201 A
$I_{S2(avg)}$	0.460 A	0.468 A	0.456 A
$I_{S3(pk)}$, $I_{S4(pk)}$	0.432 A	0.442 A	0.418 A
$I_{S3(RMS)}$, $I_{S4(RMS)}$	0.216 A	0.220 A	0.209 A
$I_{S3(avg)}$, $I_{S4(avg)}$	0.138 A	0.147 A	0.133 A

Figure 12b represents the voltages across PVG1 and PVG2. As expected, the converter operation with a fixed duty ratio of 50% enables voltage equalization. In turn, Figure 12c illustrates the current through the BBB converter inductor from the group PVG1. As predicted by theory, it results from the difference between the currents of the PV modules adjacent to the inductor, with the theoretical value of 550 mA closely aligning with the measured value of 544 mA.

Figure 12d shows the voltage, power, and current waveforms before and after the operation of the proposed converter. Initially, the load is set to operate at the MPP of the PV string without the proposed topology. In this case, the maximum output power is 36 W at an irradiance of 1050 W/m² and a temperature of 45 °C. After activating the topology, the harvested power increases to 49.6 W, resulting in an increase of 13.6 W, or 37.8%. Additionally, the efficiency increases from 72% to 99.2%.

3.2. DPP Converter Applied to Larger PV Strings and Distinct Mismatch Conditions

The proposed architecture was applied to the six- and eight-module strings shown Figure 13a,b, respectively, connected to a variable resistor set to achieve the MPP. Due to limited resources, the tests were conducted through simulations in Simulink rather than experimentally.
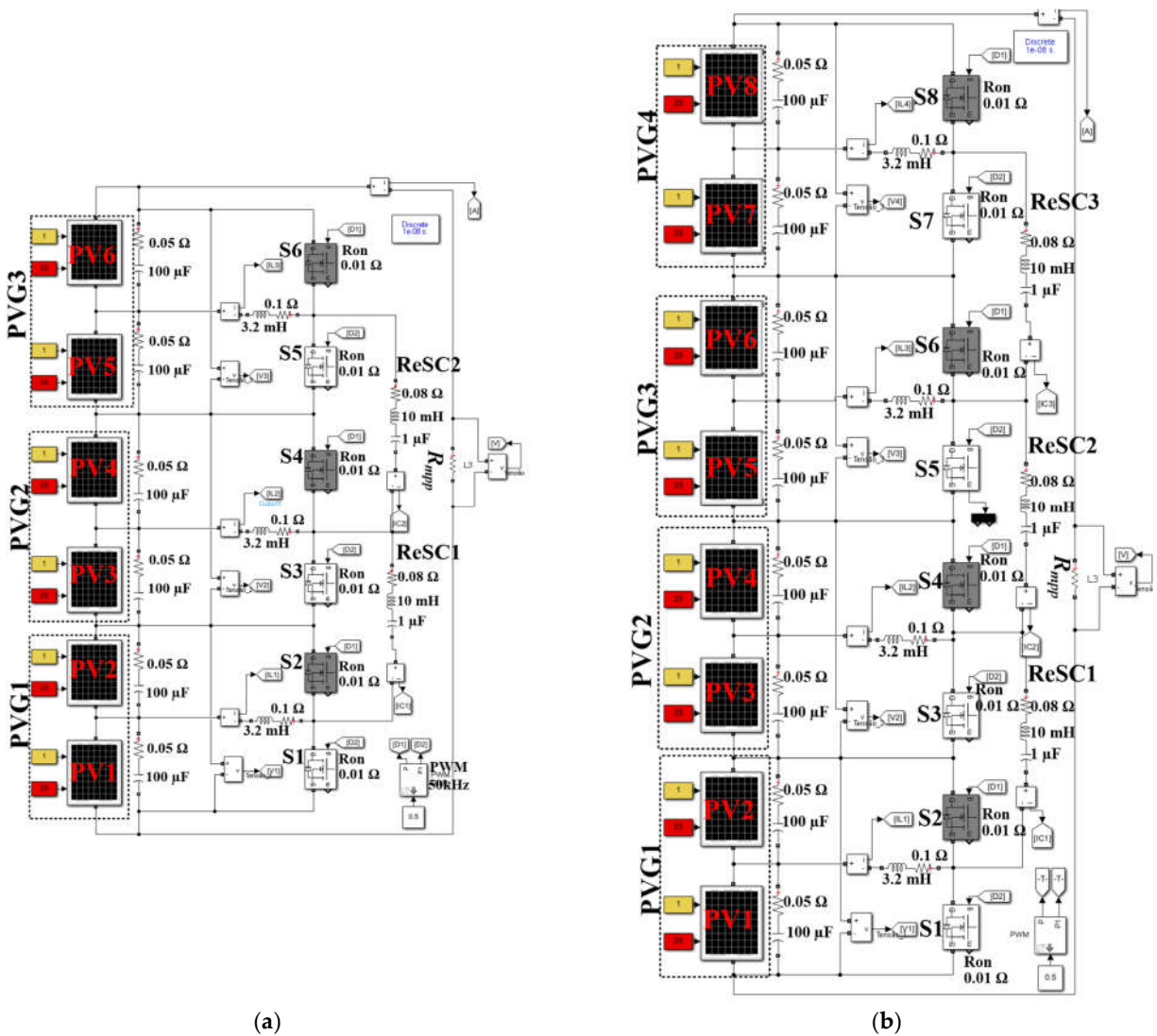
(**a**)   (**b**)

Figure 13. Proposed architecture associated with: (a) a six-module string and (b) an eight-module string.

3.2.1. Six-Module String

The first scenario comprises two 20 W modules in PVG1, with 10 W modules forming the other groups, resulting in a maximum available power of 80 W. The main waveforms for this condition are shown in Figure 14. Since all modules in the groups are identical, the BBB converters will not operate, meaning the average current through the BBB converter inductors is zero. Figure 15 shows the voltage, current, and power waveforms in the string. The maximum harvested power without the proposed topology is 55.18 W. However, at *t* = 0.2 s, the converter is activated, as the power increases to 79.85 W.
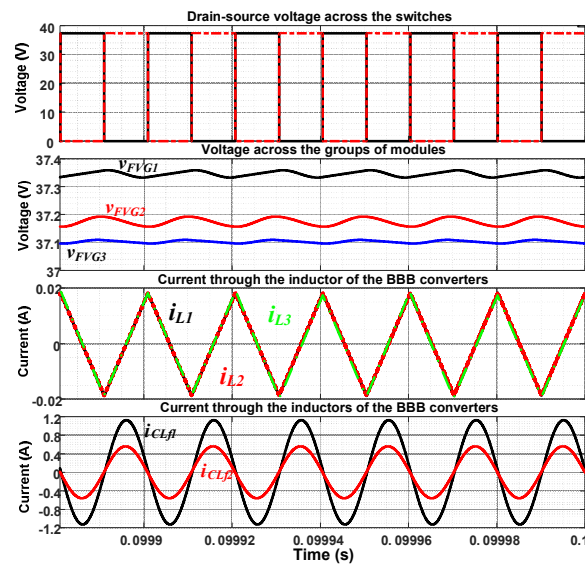
Figure 14. Main waveforms obtained in the DPP converter in the first scenario.
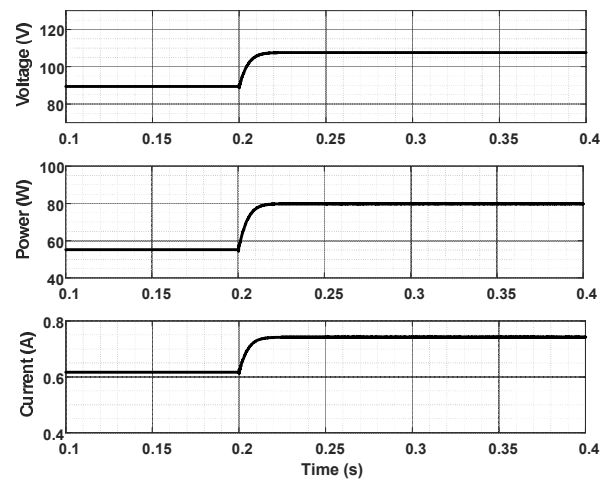

Figure 15. Voltage, current, and power obtained in the six-module PV string in the first scenario.

In the second scenario, only PV1 in the PVG1 group consists of a 20 W module, while the other elements in the string are rated at 10 W. As a result, the maximum available power is 70 W. The main waveforms for this condition are illustrated in Figure 16. Since the modules in PVG1 are mismatched, an average current of 0.55 A flows through the inductor of the BBB converter in this group. The maximum power extracted from the string without the proposed topology is 54.18 W, as demonstrated in Figure 17. However, at $t = 0.2$ s, the converter is activated, increasing the power to 69.65 W.
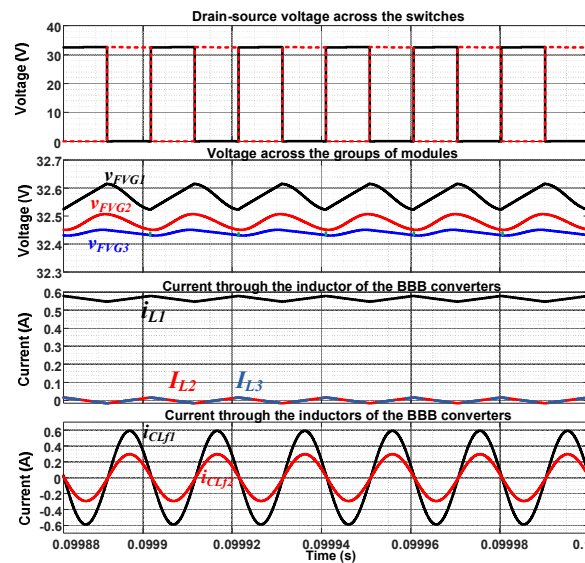
Figure 16. Main waveforms obtained in the DPP converter in the second scenario.
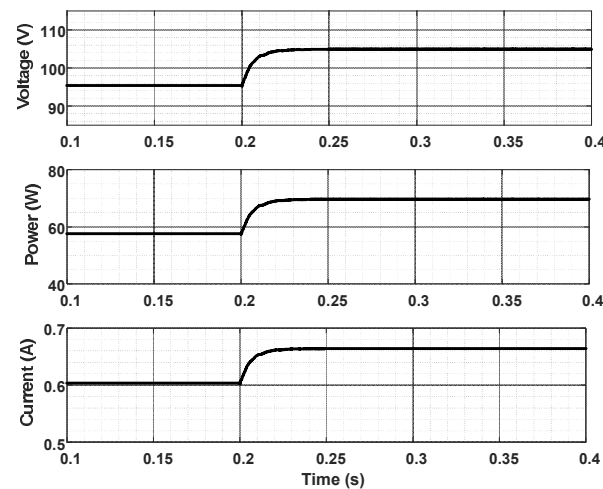

Figure 17. Voltage, current and power obtained in the six-module PV string in the second scenario.

Table 5 summarizes some key parameters describing the aforementioned simulation results. In both conditions, the DPP converter can significantly enhance energy harvesting from the string.

Table 5. Summary of the simulation results obtained from a six-module string.

| Scenario	Tracking Time	Maximum Theoretical Power	Extracted Power		Efficiency	
			Turned-off Converter	Turned-on Converter	Turned-off Converter	Turned-on Converter
#1	25 ms	80 W	79.9 W	98.8 W	79.9%	98.8%
#3	50 ms	70 W	58.0 W	90.8 W	63.0%	98.7%

3.2.2. Eight-Module String

The first scenario comprises only permanent mismatch, in which the string consists of four groups of PV modules PVG1…PVG4 operating in STC, resulting in a maximum available power of 100 W. Group PVG1 relies on two 20 W modules, whereas groups

PVG2…PVG4 employ two 10 W modules each. The waveforms in Figure 18a provide evidence that the BBB converters will not operate under this condition because the average inductor currents are null, as there is no mismatch involving the modules of a given group. Figure 18b also shows that initially the extracted power is 79.9 W, but it increases to 99.8 W after the converter is activated at *t* = 0.2 s.
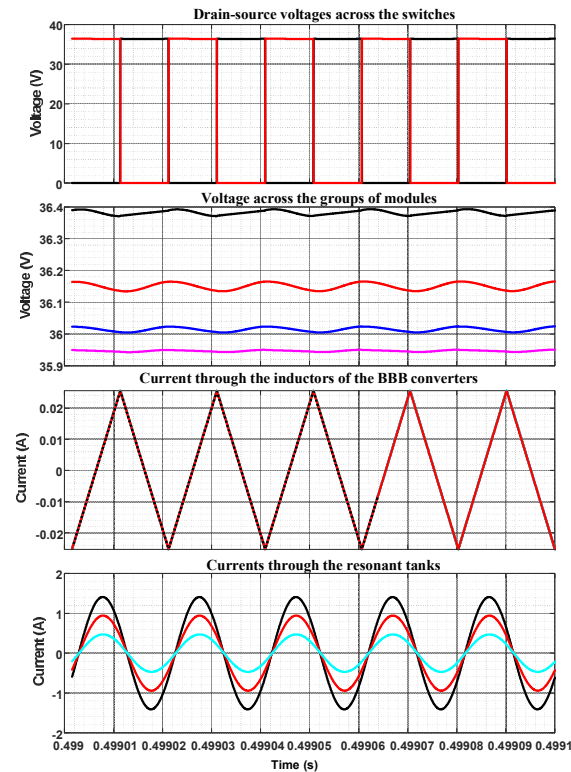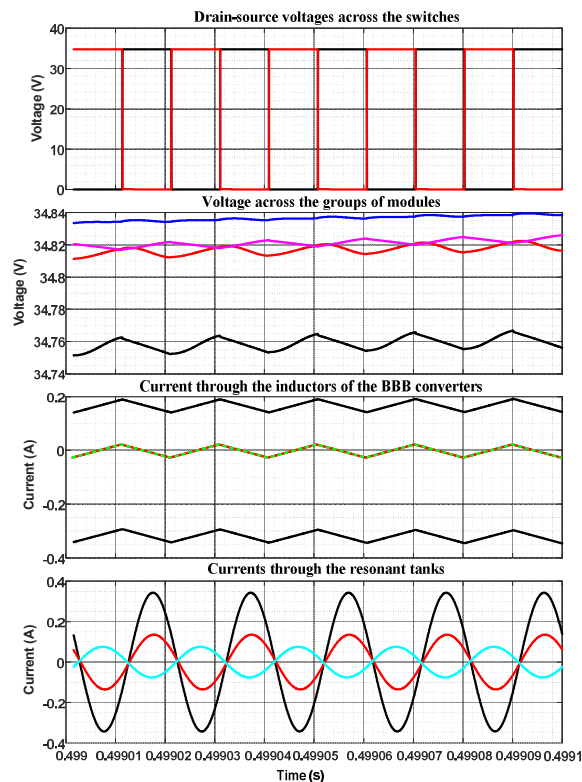

(**a**)
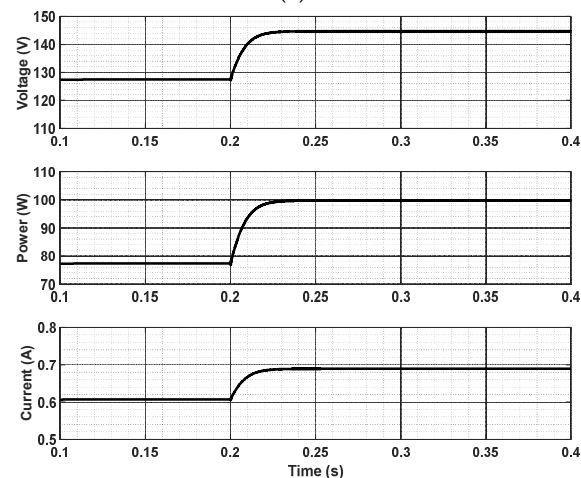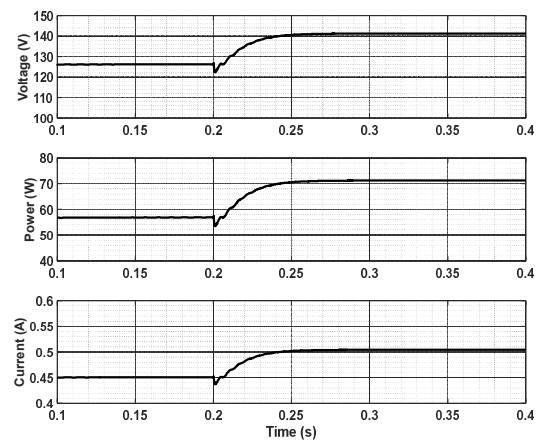

(**b**)

Figure 18. PV system under permanent mismatch conditions: (**a**) main waveforms of the BBB-ReSC converter and (**b**) voltage, current, and power of the PV string before and after the BBB-ReSC converter operation.

The second scenario involves only a temporary mismatch, with all modules being identical and rated at 10 W. Modules PV1 and PV8, belonging to groups PVG1 and PVG4, respectively, are subjected to non-uniform irradiance levels of 500 W/m² and 700 W/m². In

turn, the remaining modules operate in STC, resulting in a maximum total available power of 58.2 W. Figure 19a shows that only the BBB converters associated with PVG1 and PVG4 will operate under this condition, as these groups contain mismatched modules. After the converter is activated at *t* = 0.2 s in Figure 19b, the extracted power increases to 71.2 W.
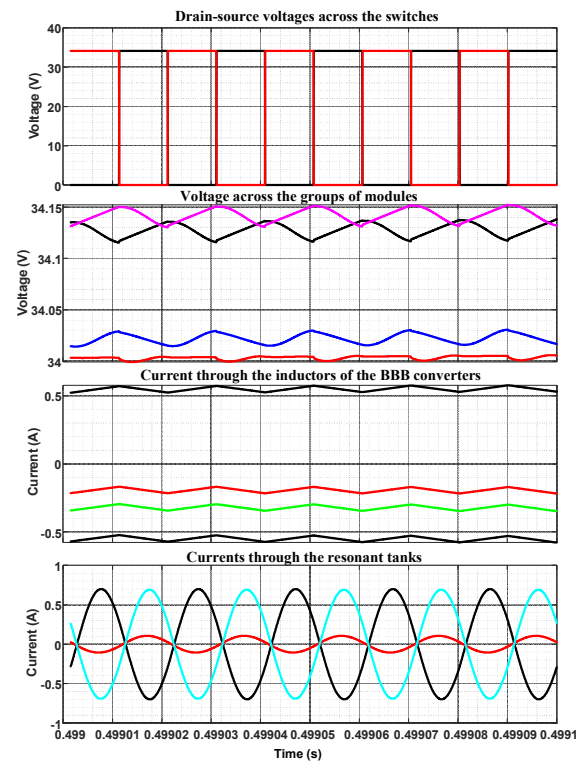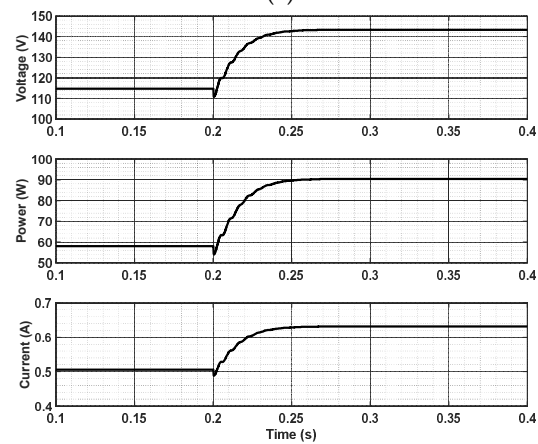

(**a**)

(**b**)

Figure 19. PV system under temporary mismatch conditions: (**a**) main waveforms of the BBB-ReSC converter and (**b**) voltage, current, and power of the PV string before and after the BBB-ReSC converter operation.

The third scenario involves a more severe condition where temporary and permanent mismatches occur simultaneously. PV1 and PV8 are two 20 W modules that belong to groups PVG1 and PVG4, respectively, while the remaining ones are rated at 10 W. Besides,

modules PV3 and PV5, associated with groups PVG2 and PVG3, respectively, are subjected to distinct irradiance levels of 500 W/m² and 700 W/m². All the remaining modules operate in STC, resulting in a maximum total available power of 58 W for the string. Figure 20a shows that all BBB converters are required to operate because all PV groups are under some sort of mismatch, either permanent or temporary. After the converter is activated at *t* = 0.2 s in Figure 20b, the extracted power increases to 90.8 W.

(**a**)

(**b**)

Figure 20. PV system under simultaneous permanent and temporary mismatch conditions: (**a**) main waveforms of the BBB-ReSC converter and (**b**) voltage, current, and power of the PV string before and after BBB-ReSC converter operation.

Table 6 presents some key parameters describing the simulation results. Overall, it is reasonable to state that the DPP converter plays a significant role in maximizing energy harvesting during both temporary and permanent mismatch conditions.

Table 6. Summary of the simulation results obtained from an eight-module string.

Scenario	Tracking Time	Maximum Theoretical Power	Extracted Power		Efficiency	
			Turned-off Converter	Turned-on Converter	Turned-off Converter	Turned-on Converter
#1	25 ms	100 W	79.9 W	98.8 W	79.9%	98.8%
#2	50 ms	72 W	58.2 W	71.2 W	80.8%	98.8%
#3	50 ms	92 W	58.0 W	90.8 W	63.0%	98.7%

3.3. Discussion

This section compares the proposed topology with two other PV-to-PV architectures: one using BBB converters [23], and a hybrid approach with BBB converters and switched capacitors, also known as the energy recovery circuit (ERC) [35]. These two structures were chosen because they are widely referenced in the literature and share similar characteristics with the solution introduced in this work. Consequently, the sizing of their components is done similarly, ensuring a fair comparison since both use identical elements. Initially, the PV string, composed of mismatched modules, operates individually without DPP converters. Then, at a given moment, the DPP converters are activated to recover energy from the PV string. This procedure allows for assessing the energy recovery, followed by a comparison between the topologies. Thus, it is possible to identify advantages, disadvantages, and applicability of such converters in specific scenarios.

For this purpose, consider a permanent mismatch condition in an eight-module string. Case 1# reflects a condition in which two 20 W modules are placed in PVG1, while the remaining elements are rated at 10 W, yielding a maximum theoretical power of 100 W. In case #2, a single 20 W module exists in PVG1 instead, corresponding to a maximum power of 90 W. The same temperature and irradiance conditions mentioned in Sections 3.1.1 and 3.1.2 are adopted in the tests.

3.3.1. Energy Recovery

Figure 21 represents the output power of the PV string for case #1, both before and after the activation of the DPP converters for the three strategies used. Between 0.3 s and 0.5 s, the PV string operates without the converters disabled, during which the maximum extracted power is 76 W. From 0.5 s to 0.7 s, the converters are activated and recover energy from the PV string. The maximum harvested power with the proposed BBB-ReSC converter is 99.8 W, while the PV-to-PV architectures with BBB and BBB-SC converters achieve 94.7 W and 99.5 W, respectively. Thus, compared to the condition in which no DPP converters are used, there is a percent energy recovery of 31.3% with the BBB-ReSC converter, 30.9% with the BBB-SC converter, and 24.6% with the PV-to-PV architecture based on BBB converters.
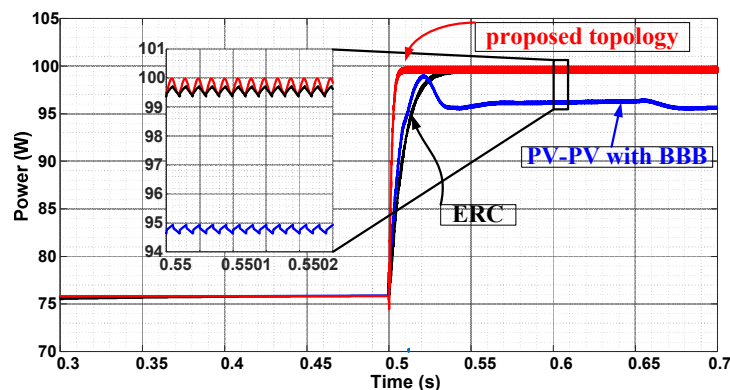

Figure 21. Energy recovery obtained with DPP converters for case #1.

Figure 22 shows the energy recovery achieved in case #2 for each topology. The maximum power harvested from the string between 0.3 s and 0.5 s is 78.5 W. After, the BBB-ReSC converter is activated, it increases to 89.65 W, accounting for a 14.2% increase. In turn, the maximum power extracted by the PV-to-PV topology with BBB converters and the ERC are 89.5 W and 87.82 W, respectively, corresponding to 14% and 11.87%.
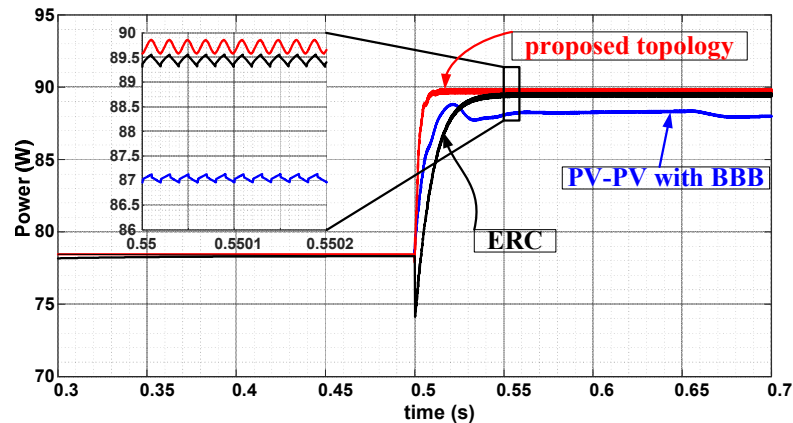

Figure 22. Energy recovery obtained with DPP converters for case #2.

3.3.2. Comparison of the Topologies

In terms of scalability, the PV-to-PV architecture based on BBB converters presents the best performance as it can be implemented with any number of modules. Additionally, the maximum voltage stress on the switches is equivalent to the sum of the voltages of the adjacent modules. However, this architecture faces two main issues: the large number of switches, totaling $2N + 2$, and the accumulation of diverted current, where N is the number of converters. These two factors significantly reduce the power extracted from the PV string, as observed in the power waveforms. In this regard, as previously discussed in the literature [27,41], this structure is particularly suitable for temporary mismatches, such as partial shading, and at the submodule level involving lower power applications.

On the other hand, the ERC does not suffer from the accumulated diverted current phenomenon. Thus, the extracted power increases significantly. As a result, this structure becomes suitable for application at the module level. However, it is important to highlight some important issues:

- Scalability: The BBB-SC converter can only be implemented with $N = 2 \cdot k$ modules, $k = 1, 2,\ldots$. This significantly reduces the applicability of the structure, making it unfeasible for strings composed of six, 10, or 12 modules, for example.
- Hard-switching operation of semiconductors: This characteristic contributes to a reduction in system efficiency, especially when high switching frequencies are required to achieve the full-scale load (FSL).
- High voltage stress on the switches of the central BBB converter: As mentioned, the voltage stress on the switches of the BBB converter experience is the sum of the voltages of the adjacent modules. Since the central BBB converter is connected between a group of modules and the main bus, the voltage across the semiconductors is equivalent to the sum of the voltages of all modules in the PV string.
- Need for high switching frequencies or large capacitors for FSL operation: To achieve the FSL, high switching frequencies are necessary, which increase switching losses. An alternative is to use large capacitors. However, this is inappropriate because electrolytic capacitors would be necessary. Such elements have a high equivalent series resistance (ESR) that affects voltage equalization in the PV string.

It is observed that the BBB-ReSC topology does not have the same level of scalability as the PV-to-PV architecture, meaning it can be implemented with $N = 2 \cdot k$ modules, $k = 1$,

2,…. However, compared to the ERC, it shows enhanced performance. Although this solution also experiences accumulated diverted current issues, this problem is significantly mitigated, as it is not as severe as in the PV-to-PV architecture. This is because this phenomenon affects only one group of two modules, which prevents high currents flowing through the semiconductors. Additionally, due to its resonant characteristic, hard-switching operation is eliminated in most cases. This is only likely to occur in specific situations, and only in the switches of the group affected by the mismatch. Given the above, the BBB-ReSC converter shows similar or even superior efficiency compared to the ERC, as demonstrated in Figures 21 and 22.

Figure 23 compares the DPP solutions discussed thus far. A limitation of the proposed topology is that, in high-power PV modules, it is necessary to connect bypass diodes at the substring level. Thus, if partial shading affects only part of the module, the distortion of the *P–V* curve will impact the operation of the DPP converter. Another important issue is the implementation cost, which becomes crucial, especially in large plants.

An interesting extension of this study could involve investigating the possibility of replacing some MOSFETs in the structure with diodes. This is feasible because, under permanent mismatch conditions, it is possible to accurately determine where the mismatch will occur. Consequently, the current flow through certain switches in the topology will consistently follow the same direction. Through a comprehensive mathematical analysis, it would be possible to evaluate the positions of the modules in the PV string that lead to decreased harvested power and reduced current stress on the converter elements, resulting in higher efficiency and lower losses.
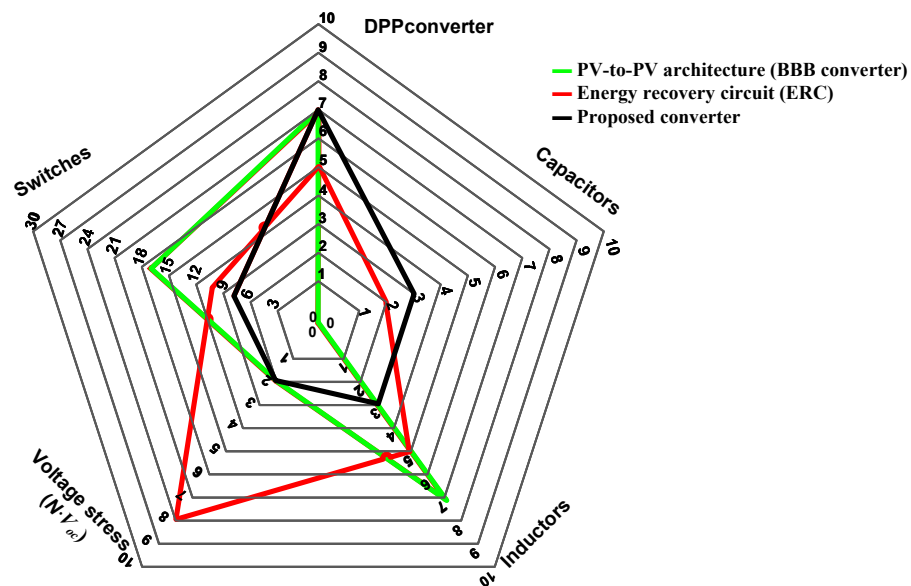

Figure 23. Comparison of DPP converters.

4. Conclusions

This work has proposed a novel DPP topology to address the issues associated with permanent mismatch. This circuit is based on a hybrid architecture, incorporating both the BBB and ReSC converters. As a result, the problems related to diverted current accumulation from the PV-to-PV architecture and high voltage stress from the PV-to-bus architecture are mitigated. Moreover, compared to other well-known topologies, the number of active switches is reduced to just one per module. An additional significant feature is the elimination of hard switching issues in the SC converter by replacing it with the ReSC converter. Consequently, the losses associated with this topology are reduced, making it suitable for applications involving permanent mismatch.

The proposed approach was analyzed to address hard-switching issues found in existing structures. A thorough mathematical analysis was conducted to determine the voltage and current stresses on the converter elements, facilitating their proper sizing. Experimental tests were performed to verify the equations and validate the operation of the proposed solution. The simulation and experimental results showed a significant energy recovery of the PV string's power. It is important to note that this recovery rate may vary depending on the mismatch level between modules, irradiance, and the number of modules in the PV string.

Author Contributions: Conceptualization and methodology, F.L.T. and E.R.R.; formal analysis and investigation, C.M.A.d.L.; supervision, F.L.T. and E.R.R; visualization, A.S.M. and K.F.Á.O.; writing—original draft preparation, C.M.A.d.L.; writing—review and editing, C.M.A.d.L. and F.L.T. All authors have read and agreed to the published version of the manuscript.

Institutional Review Board Statement: Not applicable.

Informed Consent Statement: Not applicable.

Data Availability Statement: Data are available upon request from the authors.

Conflicts of Interest: The authors declare no conflicts of interest.

References

1. Kasper, M.; Bortis, D.; Kolar, J.W. Classification and comparative evaluation of PV panel-integrated DC–DC converter concepts. *IEEE Trans. Power Electron.* **2014**, *29*, 2511–2526.
2. Dolara, A.; Lazaroiu, G.C.; Leva, S.; Manzolini, G. Experimental investigation of partial shading scenarios on PV (photovoltaic) modules. *Energy* **2013**, *55*, 466–475.
3. Niazi, K.A.K.; Yang, Y.; Sera, D. Review of mismatch mitigation techniques for PV modules. *IET Renew. Power Gener.* **2019**, *13*, 2035–2050.
4. Sherwani, A.; Usmani, J. Life cycle assessment of solar PV based electricity generation systems: A review. *Renew. Sustain. Energy Rev.* **2010**, *14*, 540–544.
5. Herrmann, W.; Wiesner, W.; Vaassen, W. Hot spot investigations on PV modules-new concepts for a test standard and consequences for module design with respect to bypass diodes. In Proceedings of the Conference Record of the Twenty Sixth IEEE Photovoltaic Specialists Conference-1997, Anaheim, CA, USA, 6 August 2000; pp. 1129–1132.
6. Ahsan, S.; Niazi, K.A.K.; Khan, H.A.; Yang, Y. Hotspots and performance evaluation of crystalline-silicon and thin-film photovoltaic modules. *Microelectron. Reliab.* **2018**, *88*, 1014–1018.
7. Vieira, R.G.; de Araújo, F.M.; Dhimish, M.; Guerra, M.I. A comprehensive review on bypass diode application on photovoltaic modules. *Energies* **2020**, *13*, 2472.
8. Guerriero, P.; Tricoli, P.; Daliento, S. A bypass circuit for avoiding the hot spot in PV modules. *Sol. Energy* **2019**, *181*, 430–438.
9. Kim, K.A.; Krein, P.T. Reexamination of photovoltaic hot spotting to show inadequacy of the bypass diode. *IEEE J. Photovolt.* **2015**, *5*, 1435–1441.
10. Motahhir, S.; El Hammoumi, A.; El Ghzizal, A. Photovoltaic system with quantitative comparative between an improved MPPT and existing INC and P&O methods under fast varying of solar irradiation. *Energy Rep.* **2018**, *4*, 341–350.
11. da Luz, C.M.A.; Vicente, E.M.; Tofoli, F.L. Experimental evaluation of global maximum power point techniques under partial shading conditions. *Sol. Energy* **2020**, *196*, 49–73.
12. Belhachat, F.; Larbes, C. A review of global maximum power point tracking techniques of photovoltaic system under partial shading conditions. *Renew. Sustain. Energy Rev.* **2018**, *92*, 513–553.
13. Shams, I.; Mekhilef, S.; Tey, K.S. Advancement of voltage equalizer topologies for serially connected solar modules as partial shading mitigation technique: A comprehensive review. *J. Clean. Prod.* **2021**, *285*, 124824.
14. Solórzano, J.; Egido, M. Hot-spot mitigation in PV arrays with distributed MPPT (DMPPT). *Sol. Energy* **2014**, *101*, 131–137.
15. Dhople, S.V.; Ehlmann, J.L.; Davoudi, A.; Chapman, P.L. Multiple-input boost converter to minimize power losses due to partial shading in photovoltaic modules. In Proceedings of the 2010 IEEE Energy Conversion Congress and Exposition, Atlanta, GA, USA, 1 November 2010; pp. 2633–2636.
16. Hasan, R.; Mekhilef, S.; Seyedmahmoudian, M.; Horan, B. Grid-connected isolated PV microinverters: A review. *Renew. Sustain. Energy Rev.* **2017**, *67*, 1065–1080.

17. Kim, K.A.; Shenoy, P.S.; Krein, P.T. Converter rating analysis for photovoltaic differential power processing systems. *IEEE Trans. Power Electron.* **2014**, *30*, 1987–1997.

18. Bell, R.; Pilawa-Podgurski, R.C. Decoupled and distributed maximum power point tracking of series-connected photovoltaic submodules using differential power processing. *IEEE J. Emerg. Sel. Top. Power Electron.* **2015**, *3*, 881–891.

19. Shenoy, P.S.; Kim, K.A.; Krein, P.T.; Chapman, P.L. Differential power processing for efficiency and performance leaps in utility-scale photovoltaics. In Proceedings of the 2012 38th IEEE Photovoltaic Specialists Conference, Austin, TX, USA, 3–8 June 2012; pp. 1357–1361.

20. Qin, S.; Barth, C.B.; Pilawa-Podgurski, R.C. Enhancing microinverter energy capture with submodule differential power processing. *IEEE Trans. Power Electron.* **2016**, *31*, 3575–3585.

21. Khan, O.; Xiao, W. Review and qualitative analysis of submodule-level distributed power electronic solutions in PV power systems. *Renew. Sustain. Energy Rev.* **2017**, *76*, 516–528.

22. Walker, G.R.; Pierce, J.C. Photovoltaic DC-DC module integrated converter for novel cascaded and bypass grid connection topologies—Design and optimization. In Proceedings of the 2006 37th IEEE Power Electronics Specialists Conference, Jeju, Republic of Korea, 18–22 June 2006; pp. 1–7.

23. Shenoy, P.S.; Kim, K.A.; Johnson, B.B.; Krein, P.T. Differential power processing for increased energy production and reliability of photovoltaic systems. *IEEE Trans. Power Electron.* **2013**, *28*, 2968–2979.

24. Karakaş, E.; Öner, Y. A modular differential power processing converter design with simplified voltage equalization for photovoltaic systems. *Electr. Power Compon. Syst.* **2024**, *52*, 1397–1413.

25. Gouvêa, E.C.; Castro, T.S.; de Souza, T.M. Performance analysis of interconnection and differential power processing techniques under partial shading conditions. *Energies* **2024**, *17*, 3252.

26. Jiang, J.; Zhang, T.; Chen, D. Analysis, design, and implementation of a differential power processing DMPPT with multiple buck–boost choppers for photovoltaic module. *IEEE Trans. Power Electron.* **2021**, *36*, 10214–10223.

27. da Luz, C.M.A.; Ribeiro, E.R.; Tofoli, F.L. Analysis of the PV-to-PV architecture with a bidirectional buck-boost converter under shading conditions. *Sol. Energy* **2022**, *232*, 102–119.

28. Chen, L.-C.; Bagci, F.S.; Kim, K.A. An improved photovoltaic differential power processing system using bidirectional boost-type converters with synchronous switching. *IEEE Trans. Power Electron.* **2024**, *39*, 16720–16730.

29. Uno, M.; Sato, H.; Oyama, S. Switched capacitor-based modular differential power processing architecture for large-scale photovoltaic systems under partial shading. *IEEE Trans. Energy Convers.* **2022**, *37*, 1545–1556.

30. Qiu, Z.; Zhao, B.; Cui, H.; Liang, B.; Huangfu, Y. A modified switched-capacitor based differential power processing converter with reduced components for substring-level photovoltaic application. In Proceedings of the IECON 2023-49th Annual Conference of the IEEE Industrial Electronics Society, Singapore, Singapore, 16–10 October 2023; pp. 1–6.

31. Jeong, H.; Cho, H.-T.; Kim, T.; Liu, Y.-C.; Kim, K.A. A scalable unit differential power processing system design for photovoltaic applications. In Proceedings of the 2018 IEEE 19th Workshop on Control and Modeling for Power Electronics (COMPEL), Padua, Italy, 25–28 June 2018; pp. 1–8.

32. Lim, J.-H.; Lee, D.-I.; Hyeon, Y.-J.; Youn, H.-S. Differential power processing converter with active clamp structure and integrated planar transformer for power generation optimization of multiple photovoltaic submodules. *IEEE Access* **2023**, *11*, 5668–5678.

33. Chu, G.; Wen, H.; Yang, Y.; Wang, Y. Elimination of photovoltaic mismatching with improved submodule differential power processing. *IEEE Trans. Ind. Electron.* **2020**, *67*, 2822–2833.

34. Zhang, W.; Li, J.; Mao, P. A novel isolated-port voltage equalizer for photovoltaic systems under mismatch conditions. In Proceedings of the IECON 2017-43rd Annual Conference of the IEEE Industrial Electronics Society, Beijing China, 29 October–1 November 2017; pp. 639–644.

35. Ramli, M.Z.; Salam, Z. A simple energy recovery scheme to harvest the energy from shaded photovoltaic modules during partial shading. *IEEE Trans. Power Electron.* **2014**, *29*, 6458–6471.

36. dos Santos, C.H.; Donoso-Garcia, P.F.; Junior, S.I.S. A comparative analysis of voltage equalizers for partial shading compensation in PV arrays. *Eletrônica Potência* **2019**, *24*, 323–335.

37. Kadri, R.; Gaubert, J.-P.; Champenois, G. Nondissipative string current diverter for solving the cascaded DC–DC converter connection problem in photovoltaic power generation system. *IEEE Trans. Power Electron.* **2011**, *27*, 1249–1258.

38. Qin, S.; Cady, S.T.; Dominguez-Garcia, A.D.; Pilawa-Podgurski, R.C.N. A distributed approach to maximum power point tracking for photovoltaic submodule differential power processing. *IEEE Trans. Power Electron.* **2014**, *30*, 2024–2040.

39. Kesarwani, K.; Stauth, J.T. A comparative theoretical analysis of distributed ladder converters for sub-module PV energy optimization. In Proceedings of the 2012 IEEE 13th Workshop on Control and Modeling for Power Electronics (COMPEL), Kyoto, Japan, 10–13 June 2012; pp. 1–6.

40. Meira Amaral da Luz, C.; Moreira Vicente, E.; Lessa Tofoli, F.; Roberto Ribeiro, E. Differential power processing architecture to increase energy harvesting of photovoltaic systems under permanent mismatch. *Sol. Energy* **2023**, *263*, 111940. https://doi.org/10.1016/j.solener.2023.111940.

41. Kasper, M.; Herden, S.; Bortis, D.; Kolar, J.W. Impact of PV string shading conditions on panel voltage equalizing converters and optimization of a single converter system with overcurrent protection. In Proceedings of the 2014 16th European Conference on Power Electronics and Applications, Lappeenranta, Finland, 26–28 August 2014; pp. 1–10.